



HAL
open science

XMM-Newton observations of the non-thermal supernova remnant HESS J1731–347 (G353.6-0.7)

V. Doroshenko, G. Pühlhofer, A. Bamba, F. Acero, W.W. Tian, D. Klochkov,
A. Santangelo

► **To cite this version:**

V. Doroshenko, G. Pühlhofer, A. Bamba, F. Acero, W.W. Tian, et al.. XMM-Newton observations of the non-thermal supernova remnant HESS J1731–347 (G353.6-0.7). *Astronomy and Astrophysics - A&A*, 2017, 608, pp.A23. 10.1051/0004-6361/201730983 . hal-01669807

HAL Id: hal-01669807

<https://hal.science/hal-01669807>

Submitted on 6 Oct 2020

HAL is a multi-disciplinary open access archive for the deposit and dissemination of scientific research documents, whether they are published or not. The documents may come from teaching and research institutions in France or abroad, or from public or private research centers.

L'archive ouverte pluridisciplinaire **HAL**, est destinée au dépôt et à la diffusion de documents scientifiques de niveau recherche, publiés ou non, émanant des établissements d'enseignement et de recherche français ou étrangers, des laboratoires publics ou privés.

***XMM-Newton* observations of the non-thermal supernova remnant HESS J1731–347 (G353.6-0.7)**

V. Doroshenko¹, G. Pühlhofer¹, A. Bamba^{2,3}, F. Acero⁴, W. W. Tian^{5,6,7}, D. Klochkov¹, and A. Santangelo¹

¹ Institut für Astronomie und Astrophysik, Sand 1, 72076 Tübingen, Germany
e-mail: doroshv@astro.uni-tuebingen.de

² Department of Physics, The University of Tokyo, 7-3-1 Hongo, Bunkyo-ku, Tokyo 113-0033, Japan

³ Research Center for the Early Universe, School of Science, The University of Tokyo, 7-3-1 Hongo, Bunkyo-ku, Tokyo 113-0033, Japan

⁴ Laboratoire AIM, IRFU/SAp – CEA/DRF – CNRS, Université Paris Diderot, Bât. 709, CEA-Saclay, Gif-sur-Yvette Cedex, France
⁵ Key Laboratory of Optical Astronomy, National Astronomical Observatories, Chinese Academy of Sciences, Beijing 100012, PR China

⁶ Institute of Astronomy and Department of Physics, National Tsing Hua University, Hsinchu, Taiwan

⁷ Department of Physics and Astronomy, University of Calgary, Calgary, Alberta T2N 1N4, Canada

Received 13 April 2017 / Accepted 5 August 2017

ABSTRACT

We report on the analysis of *XMM-Newton* observations of the non-thermal shell-type supernova remnant HESS J1731–347 (G353.6-0.7). For the first time the complete remnant shell has been covered in X-rays, which allowed direct comparison with radio and TeV observations. We carried out a spatially resolved spectral analysis of *XMM-Newton* data and confirmed the previously reported non-thermal power-law X-ray spectrum of the source with negligible variations of spectral index across the shell. On the other hand, the X-ray absorption column is strongly variable and correlates with the CO emission thus confirming that the absorbing material must be in the foreground and reinforcing the previously suggested lower limit on distance. Finally, we find that the X-ray emission of the remnant is suppressed towards the Galactic plane, which points to lower shock velocities in this region, likely due to the interaction of the shock with the nearby molecular cloud.

Key words. ISM: supernova remnants – cosmic rays – X-rays: ISM – X-rays: individuals: HESS J1731–347

1. Introduction

HESS J1731–347 (G353.6-0.7) belongs to a small group of supernova remnants (SNR) with associated TeV and non-thermal X-ray synchrotron emission from the expanding supernova shock fronts. The observed X-ray emission is evidence of relativistic TeV electrons that are accelerated in the SNR shocks. The TeV emission from HESS J1731–347 could stem from relativistic electrons (through inverse Compton emission) or, alternatively, from protons (through π^0 -decay). In order to disentangle the two processes and derive corresponding energy budgets, the parameters of the environment into which the shocks are propagating need to be known. The progenitor of HESS J1731–347 must have been a massive star as its central compact object (CCO), i.e. a neutron star is detected in its centre. Therefore, the remnant is likely surrounded by and is possibly expanding into an area of high molecular density. However, in order to achieve its current size (~ 30 pc diameter assuming a distance of ~ 3.2 kpc to the source) while still maintaining a high shock speed, the forward shock must have propagated for a large fraction of the remnant's lifetime in a tenuous medium. A likely explanation is that the remnant is expanding inside the stellar wind bubble blown by the progenitor star (Cui et al. 2016). The same scenario has also been invoked to explain the size of RX J1713.7-3946 (Berezhko & Völk 2008).

The distance to HESS J1731–347 is not firmly known up to date. It is likely that the remnant is located in one of the three

Galactic spiral arms crossing the line of sight at the near side of the Galactic centre: in the Scutum-Crux arm (at a distance of ~ 3 kpc), in the Norma arm (~ 4.5 kpc), or in the 3 kpc arm at 5–6 kpc distance. A location beyond the Galactic centre distance would imply a very high TeV luminosity and seems unlikely. A reasonable lower limit of 3.2 kpc comes from a gradient of the X-ray absorption column across the source matching the integrated gas density up to that distance, as derived from ^{12}CO and HI data (H.E.S.S. Collaboration et al. 2011). The remnant could be located on the far side of the Scutum-Crux arm, at a similar distance (in projection) of a nearby HII region at ~ 3.2 kpc distance (Tian et al. 2008); however, no morphological or other obvious link exists between the two sources. If HESS J1731–347 were located at this distance, it could be co-located with the bulk of absorbing material (i.e. inside a molecular cloud region) that is located in the Scutum-Crux arm, and possibly interact with the material. However, from the existing data, no evidence for such an interaction has been found so far.

A near distance (3.2 kpc to 4.5 kpc) is also favoured by the analysis of the X-ray spectrum of the central neutron star (Klochkov et al. 2013, 2015). Alternatively, it has been argued that HESS J1731–347 could be located in the 3 kpc arm (Fukuda et al. 2014). While the TeV profile on its own is statistically compatible with a flat profile (H.E.S.S. Collaboration et al. 2011), Fukuda et al. (2014) have argued for a partial correlation of the TeV profile with an azimuthal gas profile in the projected direction towards the SNR in the 3 kpc arm distance range. The

TeV emission has been interpreted in this scenario by a blend of hadronic emission (correlated with the gas density) and leptonic emission. Fukuda et al. (2014) also favoured this scenario based on the spatial distribution of the surrounding molecular clouds. Finally, using the roughly flat TeV azimuthal profile, Nayana et al. (2017) argued that the remnant is likely not expanding in an anisotropic medium as would be expected from molecular clouds. They then used indications for an anti-correlation with 325 MHz radio synchrotron emission to argue that the TeV emission is due to electrons, explaining the differences as being due to different magnetic field strengths and correspondingly different synchrotron burnoff energies of the radiating electrons.

Cui et al. (2016) have shown that within a framework to model the SNR evolution and associated particle acceleration, it is difficult to obtain a hadronic TeV emission scenario for HESS J1731–347 independent of the actual distance to the SNR. From the upper limit in the GeV band derived with *Fermi-LAT* (Acero et al. 2015) it was argued as well that the TeV emission from HESS J1731–347 should be leptonic dominated. However, the same arguments that have been used by Gabici & Aharonian (2014) to model the GeV–TeV emission of RX J1713.7–3946 as hadronic emission could also be applicable to HESS J1731–347. The steep GeV spectrum on its own therefore does not provide a definite discrimination between the emission models.

X-ray data of HESS J1731–347 can be used to probe the surrounding geometry of the remnant and to explore the different emission scenarios. A full sensitive X-ray coverage of the SNR has not been achieved before; the ROSAT soft X-ray survey has only revealed few photons from the source (Tian et al. 2008). So far, an *XMM-Newton* pointing towards the north-east and two *Suzaku* pointings towards the north-west and south-west of the remnant have been analysed in view of the SNR (Tian et al. 2010; H.E.S.S. Collaboration et al. 2011; Bamba et al. 2012). The *XMM-Newton* data have revealed the absorption pattern mentioned above, which has been confirmed with *Suzaku*. No thermal emission has been found from the spectral analysis of the data. The photon index of the power-law model fitted to various subregions of the remnant has been reported to vary between 2 and 3, so far without a clearly identified morphological pattern. Bamba et al. (2012) have found one region with a particularly hard index (~ 1.8); however, the angular resolution of the telescope might have masked the contribution from strong point sources to the spectrum.

For the work presented in this paper, we have obtained and analysed data from *XMM-Newton* covering the full SNR extent. For the first time, we provide a full X-ray image of the remnant (see Fig. 1) as well as a consistent spectral analysis across the source. The image has been divided into a grid of eighteen source regions (with three background regions), and the corresponding spectra have been used to analyse the spatial variations of the X-ray source parameters across the remnant. The data permit the X-ray map to be compared with the sky maps in the TeV, radio, and submillimetre bands. The analysis of the *XMM-Newton* data has been hampered to some degree by the presence of significant stray light coming from a nearby source (likely 1RXS J173157.7–335007) and Galactic ridge emission. An extensively tuned analysis has therefore been performed to deal with that problem, which is described below. The paper is organised as follows: in Sect. 2 the *XMM-Newton* data set and analysis is described in detail; Sect. 3 deals with connection of the obtained results between X-ray and other bands; and Sect. 4 summarises the conclusions.

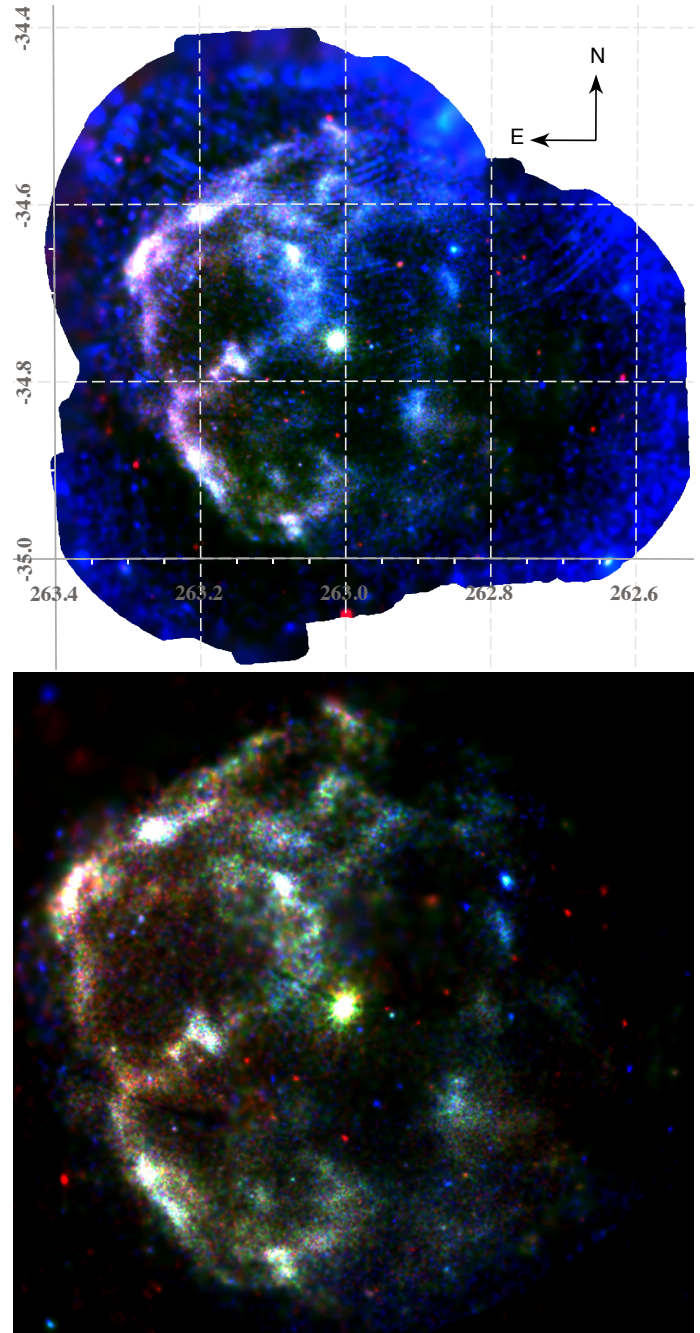


Fig. 1. Pseudo-colour mosaic image of all observations showing 0.4–1.8 keV (red), 1.8–2.8 keV (green) and 2.8–10.0 keV (blue) rates corrected only for the residual proton background (*top panel*), and central part of the same image corrected for all identified background components (*bottom panel*). All images are presented in equatorial coordinates shown in a grid in the top image. The scale of the uncorrected image has been adjusted to emphasise the contamination by stray light (mostly seen in blue) and extended emission towards the western part of the remnant. Note that the stray-light contamination is even more severe in individual observations as the location of the single reflection arcs is sensitive to the pointing of telescope.

2. Data analysis

2.1. Observations and data reduction

The remnant and the CCO have been observed with *XMM-Newton* several times. The list of observations is presented in Table 1. For data screening and reduction the *XMM SAS* version

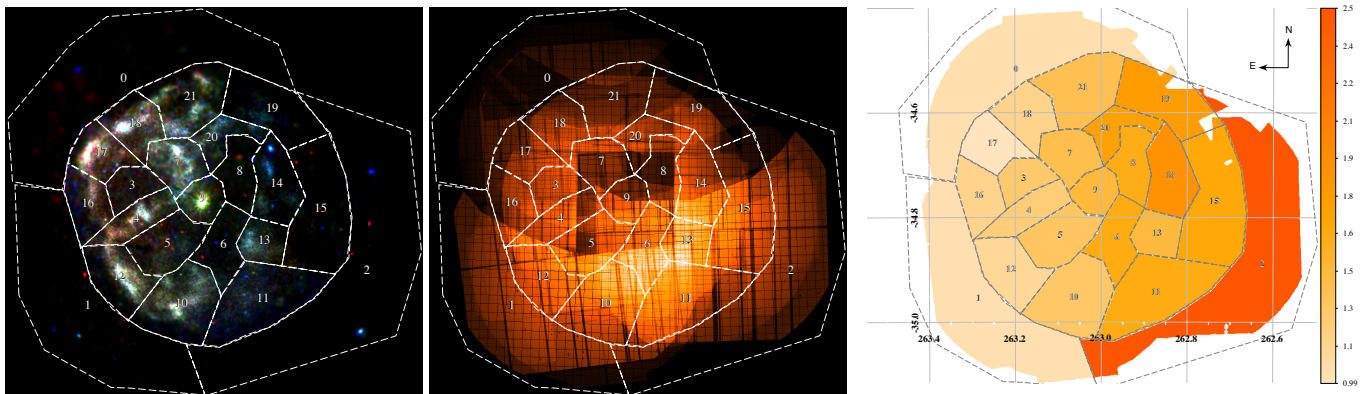


Fig. 2. *Left panel:* mosaic pseudo-colour image in 0.4–1.8 keV (red), 1.8–2.8 keV (green), and 2.8–10 keV (blue) energy bands corrected for particle, soft proton, and residual stray-light contamination. The definition of regions used for spectral analysis is also shown. *Middle panel:* combined exposure map in 0.4–10 keV band where regions most heavily contaminated by stray light and excluded from the analysis can be identified. *Right panel:* colour-coded absorption column density.

Table 1. *XMM-Newton* observations of HESS J1731–347.

Observation ID	Observation date	Duration, ks	Exposure (M1/M2/PN), ks
0405680201	2007-Mar.-21	25.4	22.5/22.9/12.1
0673930101	2012-Mar.-02	23.7	21.9/21.8/0
0694030101	2013-Mar.-07	72.4	53.1/54.9/42.5
0722090101	2013-Oct.-05	61.3	53.3/54.1/41.6
0722190201	2014-Feb.-24	131.2	88.4/97.4/0
Total		314	239.2/251.1/96.2

Notes. The “Exposure” column reflects the effective imaging exposures for each camera (EPIC MOS1, MOS2, and PN). Zero exposure means that PN was operated in timing mode.

20141104_1833-14.0.0 was used (this version also includes the formerly independent extended source analysis software package ESAS). For the analysis of extended emission from the remnant we followed the procedures described in the ESAS Cookbook¹ unless stated otherwise. We excluded data taken in windowed and timing modes, and only considered observations performed in imaging mode. We also excluded data from CCD chips operating in the “anomalous mode” characterised by a high level of noise at low energies, and screened the data for periods of enhanced orbital background (using the ESAS tasks *mos/pn-filter* with default filtering criteria).

Inspection of the images extracted from the screened data immediately revealed that all observations are affected by stray light from a nearby bright source (likely 1RXS J173157.7–335007) to some extent. The X-ray stray light in the EPIC cameras is mainly produced by single reflections of rays coming from outside of the field of view from the hyperbolic section of the mirrors and is detected as spurious arc-like structures across large fractions of the detector area. Fortunately, the projection of these onto the sky plane changes from camera to camera and also with pointing direction. Therefore, even after visual-based exclusion of the regions contaminated by stray light, the remnant was still completely covered by observations, although the exposure was reduced, as can be seen in the cumulative exposure map presented in Fig. 2.

¹ <http://heasarc.gsfc.nasa.gov/docs/xmm/esas/cookbook/xmm-esas.html>

Our study is focused on the extended emission of the remnant shell, so the contribution of the point sources must be removed. To detect the point sources, for each observation and camera (i.e. each individual exposure) we extracted images and ran the SAS source detection pipeline (using both *eboxdetect* and *emldetect* tasks) for four energy bands: 0.4–1.8, 1.8–2.8, 2.8–10, and 0.4–10 keV. In addition, we followed the same procedure for the combined mosaic image including all observations. All detected sources were then merged into a single list, which was then manually screened to exclude the spurious detections corresponding to bright shell filaments. The final source list consisting of 110 sources was then used to mask the point sources for both imaging and spectral analysis (using the *region* task to define exclusion regions containing 95% of flux for each source).

We also used the multi-colour mosaic presented to define source extraction regions for spectral analysis. We considered both variation in total intensity and colour (i.e. source intensity in individual energy ranges) to define the 22 regions matching the observed structure of the shell and the background in order to investigate spatial variations of the spectrum across the remnant (see Fig. 2).

For each observation and telescope we derived the spectral products (i.e. source and in-orbit particle background spectra and respective response files) for visible regions using the SAS tasks *mos/pn-spectra*. In total, 167 spectra with a mean exposure of ~42 ks were derived. For each spectrum, the exposed sky area (excluding areas contaminated by stray light and point sources, gaps between individual CCD chips, and bad pixels) and scaling for the residual soft proton contamination (see the next section) were calculated using the task *proton_scale*.

2.2. Spatially resolved spectral analysis

A spectral analysis of extended source emission requires careful modelling of the background. We estimated the contribution of the in-orbit particle background and out-of-time events (for EPIC PN) based on the count-rate in the unexposed detector areas using the SAS tasks *mos/pn-back* and subtracted resulting spectra from all observed spectra. To estimate the local cosmic background, we used the source-free regions 0, 1, 2 (only available in observations 0405680201, 0694030101, and 0722090101, respectively, i.e. those with pointings displaced from the shell centre).

The source resides in the Galactic plane, so the cosmic background is expected to be dominated by the Galactic ridge emission

of unresolved point sources (*GRXE*; Revnivtsev et al. 2006). As recently discussed by Yuasa et al. (2012), the 2–50 keV X-ray spectrum of the *GRXE* can be represented with an absorbed two-temperature collisional ionisation equilibrium plasma (CIE) model with temperatures of ~ 1.5 keV and ~ 15 keV. We found that the observed local background in our observations in the 0.4–10 keV energy range is well described with an absorbed single-temperature CIE model with $kT \sim 0.7$ keV (see also Table 2). The discrepancy in the derived temperature value is not surprising taking into account the difference in energy range and likely spatial variation of spectral properties of the ridge emission and, as we verified, has little effect on the derived parameters of the shell spectrum. We also verified that the choice of the absorption model does not affect other parameters and use the *wabs* model (Morrison & McCammon 1983) throughout the paper.

The contribution from the local hot bubble (which is also expected to have $kT \sim 0.7$ keV, but is not expected to be absorbed) and from background AGN were not formally required by the fit. However, to avoid a possible bias for other parameters, we still included the well-studied AGN background as a fixed absorbed power law with an absorption column density linked to that in a given region (which is comparable with the Galactic absorption column in the direction of the source), a photon index of $\Gamma = 1.46$, and a scaled normalisation of 4.6×10^{-7} photons $\text{keV}^{-1} \text{cm}^{-2} \text{s}^{-1} \text{arcmin}^{-2}$ at 1 keV (Cappelluti et al. 2009). The actual sky area from which individual spectra were extracted differs between observations, so all model components were scaled to unit area with a scaling constant calculated using the *proton_scale* task.

We found also that despite the exclusion of the enhanced orbital background periods, a residual soft-proton contamination remained noticeable in all observations and, in fact, given the low surface brightness of the remnant, is a major background component. Therefore, we included a power law (or a broken power law if required) not folded through the instrumental response in the model to account for it. The normalisation of this component is known to depend on the position in the detector plane. However, the relative normalisation for two arbitrary regions can be calculated using the task *proton_scale* based on calibration observations. Therefore, we fit the parameters of this component only for a single arbitrarily chosen sky region in each observation, and scale it for all other regions using the scaling calculated with *proton_scale*.

Emission from the remnant itself had been reported to be non-thermal with a pure power-law spectrum, possibly with spatially varying photon index (Bamba et al. 2012). To model the source emission, we therefore used a power law with independent normalisation and photon index for individual sky regions. Once the general shape of the background spectrum was established, we included all sky regions and fitted the source and background components simultaneously to improve counting statistics. As already mentioned, two observations including the longest one were centred on the CCO and contain no source-free regions to estimate the background (including the residual soft-proton background). This is another reason why we fit all spectra from all observations simultaneously. The parameters of the source and cosmic background spectra were assumed to be linked to a given sky region, and parameters of the soft proton background to a given camera and observation. For modelling we used the *sherpa*² spectral fitting package from the *Chandra* interactive analysis of observations (CIAO v 4.7) software.

Table 2. Spectral extraction region parameters and best-fit results assuming a pure power law with constant index for all regions.

Parameters common to all regions				
Γ_{SNR}				2.66(1)
$F_{\text{SNR},2-10}$				$3.77(7) \times 10^{-11} \text{ erg s}^{-1} \text{ cm}^{-2}$
Γ_{Stray}				1.54(1)
$kT_{\text{CIE,Ridge}}$				0.74(1)
$\chi^2_{\text{red}}/\text{d.o.f.}$				1.03/20227
Region specific parameters				
Reg.	Area ^a	nH ^b	$F_{\text{SNR},2-10}^c$	$F_{\text{stray},2-10}^c$
0	272.3	1.11(3)	-	6.9(4)
1	233.1	1.06(2)	-	1.25(8)
2	326.1	3.0(2)	-	7.1(5)
3	24.3	1.16(2)	0.57(4)	0.0020(2)
4	31.6	1.21(1)	2.6(1)	0.76(5)
5	44.2	1.29(2)	1.7(1)	0.25(2)
6	36.1	1.6(3)	0.83(7)	0.37(2)
7	33.1	1.44(2)	3.8(2)	2.4(2)
8	32.1	1.68(6)	0.50(0)	0.75(5)
9	22.3	1.44(2)	1.0(1)	0.67(4)
10	66.1	1.297(1)	4.7(2)	0.005(4)
11	80.5	1.53(2)	2.3(1)	0.007(5)
12	44.7	1.14(1)	3.7(1)	0.004(3)
13	25.3	1.49(2)	1.24(8)	0.63(4)
14	44.9	1.93(4)	1.2(1)	2.1(1)
15	94.2	1.59(5)	0.30(2)	2.1(1)
16	33.9	1.1(2)	1.5(1)	0.065(4)
17	33.3	1.02(1)	2.4(2)	1.6(1)
18	36.4	1.21(2)	3.0(2)	2.4(2)
19	61.0	1.95(9)	0.90(3)	3.8(2)
20	25.1	1.81(5)	1.5(1)	1.22(8)
21	60.1	1.41(2)	3.9(3)	2.5(2)

Notes. ^(a) In units of arcmin^2 , ^(b) in units of $10^{22} \text{ atoms cm}^{-2}$, ^(c) in units of $10^{-12} \text{ erg cm}^{-2} \text{ s}^{-1}$.

Initially we found that the shell spectrum significantly hardened in the northern part of the remnant. However, the same area is most heavily contaminated by stray light. Some excess emission is also evident throughout most of the image, and in particular in the northern background region. It is clear, therefore, that stray-light contamination is not limited to the apparent arc-like structures (and their immediate neighbourhood) already excluded from the analysis, but extends much further and might even be present in exposures with no visible sign of stray-light contamination. A more conservative spatial filtering of all possibly contaminated areas would imply dropping the entire northern half or even two-thirds of the remnant from the analysis, so we opted to treat the residual stray-light contamination as an additional background component.

The energy dependence of the effective area is not calibrated for stray light, so it is not trivial to model this component. Furthermore, the degree of contamination likely differs between individual observations for the same sky region, which implies that for each spectrum an additional free parameter must be constrained. We found, however, that a single power law with a photon index of ~ 1.5 and a normalisation only variable between individual sky regions but not between individual spectra allows all spectra to be fit. Unfortunately, the normalisation of this component is also strongly correlated with the photon index of the remnant spectra, so the spectral index of the extended

² <http://cxc.harvard.edu/sherpa4.4/>

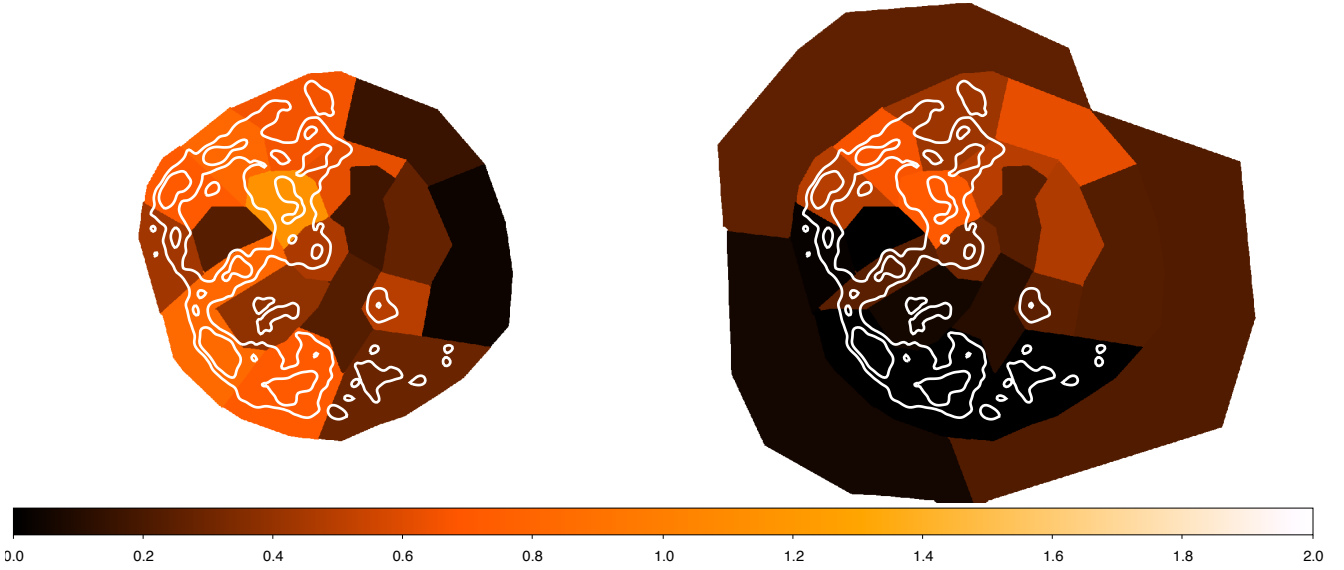


Fig. 3. Average surface brightness of the SNR emission (*left*) and residual stray-light contamination (*right*) in units of $10^{-13} \text{ erg cm}^{-2} \text{ s}^{-1} \text{ arcmin}^{-2}$ in the full (0.4–10 keV) energy range. The stray-light emission spectrum is substantially harder, so it has a factor of two higher energy flux for a given photon flux. Surface brightness roughly correlates with the reduction of exposure due to exclusion of the most heavily polluted regions shown in Fig. 2. The contours show equal brightness levels for the extended emission for reference.

emission remains unconstrained for individual regions. Moreover, the remnant is located close to the Galactic plane, so an additional contribution from the Galactic ridge X-ray emission (GRXE) is expected. The spectrum of the ridge consists of a number of emission lines and a power-law continuum with photon index of ~ 2 , close to that of the remnant. The intensity and spectrum of the GRXE are known to depend on the Galactic coordinates (Valinia & Marshall 1998; Revnivtsev et al. 2006; Ebisawa et al. 2008), and the vertical scale of the disc component of the GRXE of $\sim 1.5^\circ$ (Revnivtsev et al. 2006) is comparable to the extension of the SNR. We attempted to include this component in the fit as well. However, it was impossible to disentangle the contribution of the three power-law continua with similar indices in individual regions. Therefore, we had to conservatively assume constant photon indices across the remnant for both the SNR and residual contamination from stray light/ridge emission (referred to simply as stray-light contamination). The average surface brightness of source and residual contamination emission are shown in Fig. 3 on the same scale. We note that while the residual contamination appears relatively strong, the SNR emission is significantly softer than the stray-light emission, so the SNR emission dominates the photon flux in all energy ranges where it is actually detected. The resulting fit is statistically acceptable. However, it is still possible that we have overestimated the stray-light contribution in some regions.

It is also important to emphasise that we cannot exclude a spatial variation of the SNR spectrum as it can be masked by changes in the normalisation of the stray-light component. In order to verify that the photon index is indeed stable throughout the shell we conducted a simplified but more straightforward analysis for the brightest parts of the shell. In particular, for several bright knots shown in Fig. 4, for each observation and instrument we extracted spectra from small circular regions with radii of $50''$, comparable with the *XMM-Newton* point spread function (PSF), and associated backgrounds from annuli centred on the same position with inner and outer radii of $60''$ and $100''$, respectively. We visually inspected individual images to exclude spectra where either source or background regions were severely

affected by stray light or were close to the edge of the field of view. The remaining spectra were then modelled with an absorbed power law after subtracting the background and grouping to 100 counts per energy bin. We kept the absorption column free, as it is quite clear from the optical extinction analysis presented in Sect. 3.4 that it varies on scales as small as $\sim 1'$. The best-fit results are presented in Fig. 4. While there is some scatter in the measured photon index values, they seem to be consistent with each other within the uncertainties. The distribution of measured photon indices is also compatible with that reported based on *Suzaku* data (Bamba et al. 2012), as follows from the high two-tailed p -value of 0.81 for the two-sample Kolmogorov-Smirnov test. On the other hand, the average value is somewhat lower than that measured using the entire shell (although the deviation is not significant). There are several reasons for this offset, for example, a variation in the absorption column within larger regions used above, the presence of unabsorbed components in the background (i.e. the local bubble) unaccounted for in the simplified filament analysis, an overestimation of the stray-light contribution for the analysis of the entire shell, or a combination of the above. It is important to note, however, that the obtained results still seem to be robust despite the apparent complexity of the analysis as justified by the clear correlation of the deduced absorption column with the optical extinction described in Sect. 3.2. We also do not expect these factors to significantly affect the flux estimates, so this issue does not affect any of our conclusions. To resolve it completely, additional observations with *Chandra* which seem to be less susceptible to stray light will, however, be required.

The final fit results are presented in Table 2. All uncertainties are at the 1σ confidence interval unless stated otherwise. Flux uncertainties are estimated from a sample of 2×10^4 simulated spectra with parameters distributed according to the best-fit results, i.e. they are not affected by absorption. An example of a representative spectrum from region 21 which contains both significant source and background contributions modelled as described above is presented in Fig. 5.

The spatially resolved spectral analysis presented above is also essential for correcting the mosaic image presented in Fig. 2

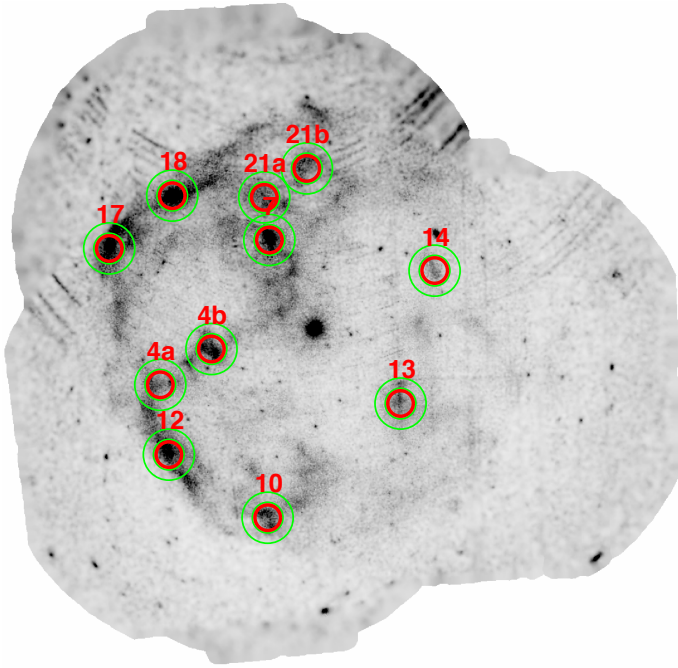


Fig. 4. Definition of source and background regions used to probe variations of the photon index across the remnant (*top*, the image is in the 0.4–10 keV band, adaptively smoothed and corrected for exposure and quiescent particle background) and the best-fit values of the photon index for each region (*bottom*, 1σ uncertainties). The dashed line represents the mean value and the shaded area corresponds to the photon index estimated using entire shell. For consistency, the region names correspond to the larger regions introduced in Fig. 2.

for the residual quiescent particle background (QPB), residual soft proton, and stray-light contamination. Using the obtained best-fit parameters we created the quiescent particle background and residual soft proton contamination images for each exposure using the *mos/pn-spectra* and *proton* tasks. The resulting images were then merged using the task *merge_comp_xmm* to obtain mosaics covering the entire remnant. To account for the residual stray-light contribution, we followed a similar approach generating mosaic images based on the expected number of contaminating photons. In particular, the average stray-light count rate in each region and energy range was calculated based on the best-fit parameters presented above, and then multiplied by the observed exposure maps to estimate the expected number of stray-light photons in each sky pixel. The resulting count images

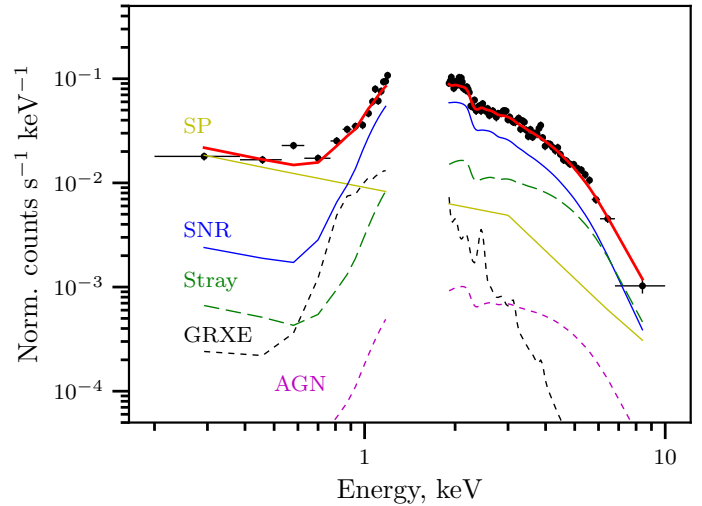


Fig. 5. Representative QPB subtracted spectrum extracted from region 21 using the MOS2 data from observation 0722190201 (black points). Identified source and residual background components described in the text are also shown as labelled in the figure.

for the quiescent particle, soft proton, and stray-light backgrounds were then co-added and subtracted from the combined net image. The final image was corrected for uneven exposure and smoothed. The absorption-corrected image presented in Fig. 9 was smoothed using a Gaussian kernel with constant width of $0.3'$. The same image without the correction for absorption presented in Figs. 2 and 1 was adaptively smoothed using the task *adapt_merge* to contain at least 300 counts per pixel in each band.

3. Discussion

3.1. Spectral energy distribution

The broadband spectral energy distribution (SED) of the SNR has been discussed by several authors (H.E.S.S. Collaboration et al. 2011; Yang et al. 2014; Acero et al. 2015) based on integrated TeV and radio fluxes and X-ray flux detected from the eastern half of the remnant scaled by a factor of two. The latter assumption implies that the X-ray flux was significantly overestimated as *XMM-Newton* observations have revealed that the eastern part is, in fact, much dimmer. The source is not detected in the GeV band which could be useful to discriminate between leptonic and hadronic TeV emission. Acero et al. (2015) obtained stringent upper limits from *Fermi* data which were interpreted as favouring a leptonic scenario. Here we present an updated spectral energy distribution fit using the X-ray flux integrated over the entire remnant, and assuming a simple single zone synchrotron-inverse Compton model. It is important to emphasise that this is probably an oversimplification as both radio and X-ray emission clearly show variation of intensity/power-law slope (Nayana et al. 2017) over the remnant. However, the quality of radio, X-ray, and TeV data does not permit a more detailed analysis at this stage, so we stick to the model used in previous investigations to facilitate the comparison of the results. Fitting and modelling of the SED were carried out using the *naima* package (Zabalza 2015).

In addition to the updated X-ray flux estimate, we include the new measurement at 325 MHz by Nayana et al. (2017) and the radio fluxes at 1.4 and 5 GHz reported by Tian et al. (2008). We also included an additional seed photon component associated with the optical star located close to the centre of the remnant with a temperature of 9×10^4 K and a density of 0.02 eV cm^{-3}

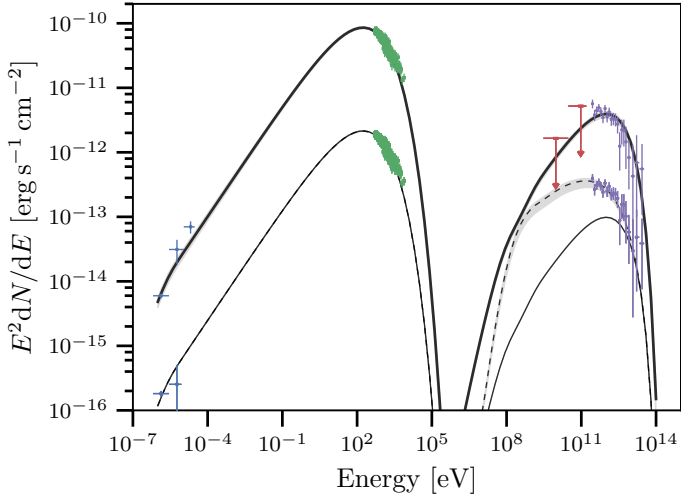


Fig. 6. Broadband spectral energy distribution (SED) and the best-fit leptonic scenario model (upper set of lines). The X-ray spectrum used here is a simulated *PN* spectrum with an exposure adjusted to yield the same spectral index and flux uncertainties as the best-fit result presented in Table 2 (i.e. the flux is integrated over all extraction regions with the contribution of point sources removed). The lower set of lines shows the SED scaled to represent fluxes within region 19 and the corresponding leptonic model with all parameters fixed to that from a global fit. The same model with an additional hadronic component accounting for the excess TeV flux is also shown for illustration (dashed line).

(Doroshenko et al. 2016), which was not included in the fits by Acero et al. (2015). The best fit presented in Fig. 6 yields values similar to those reported by Yang et al. (2014) with an electron population index of $s_e = 1.85(1)$ and a cut-off at 11.2 TeV, background field of $B = 23(1) \mu\text{G}$, and an electron population energy above 1 GeV of $W_e = 0.20(1) \times 10^{48}$ erg (again assuming a distance of 3.2 kpc).

The derived magnetic field is consistent with earlier estimates and seems to be rather low compared with other young SNRs. Indeed, fields derived from thin X-ray filament structures or the time variation of X-ray emission were found to be significantly higher in some cases (a few 100 μG ; Bamba et al. 2003, 2005; Uchiyama et al. 2007). On the other hand, the filaments in HESS J1731–347 do not seem to be as sharp as in those cases, and rather clumpy, i.e. they are more similar to those in RCW 86 (whose age is ~ 2000 yr; Bamba et al. 2005). The magnetic field in this SNR can thus indeed be lower than in other younger SNRs, which would also support a leptonic origin for the bright VHE gamma-rays.

It is important to note that the single-zone SED model considered above is almost certainly an oversimplification. Indeed, as discussed by Nayana et al. (2017) and below in Sect. 3.3, the morphologies of radio, X-ray, and TeV shells are significantly different. Furthermore, based on the comparison of 325 and 610 MHz fluxes, Nayana et al. (2017) reported slightly different spectral indices for the eastern and western parts of the radio shell. In particular, the spectrum of the brighter eastern part was found to be somewhat steeper, which, together with the spatial anticorrelation of radio and TeV brightness, was interpreted as evidence for a stronger ambient magnetic field in this region.

We also considered, therefore, modelling of the SED of the north-western part of the shell only, where the difference in radio/X-ray and TeV morphologies is most apparent. It is important to emphasise, however, that the quality of the data in all bands is not sufficient for a detailed spatially resolved analysis of

the SED and the estimates below are thus very approximate and serve mainly an illustrative purpose.

For the estimates we consider region 19 defined for our X-ray analysis, which roughly corresponds to the radio filament 3 reported by Nayana et al. (2017). We estimate that X-ray, radio, and TeV fluxes from this part of the shell roughly correspond to ~ 3 , 2.5, and 7% of the total source flux. To estimate the TeV flux we used the ratio of excess counts from region 19 to that from the entire remnant using the image from H.E.S.S. Collaboration et al. (2011), and scaled the spectrum reported there using this value. Similarly, we re-scale the X-ray spectrum used for the global SED analysis to flux measured from region 19 as a rough estimate. The resulting SED is presented in Fig. 6 along with the global SED and a leptonic model with all parameters except the normalisation fixed to global values.

As can be seen from the figure, the model in this case significantly underpredicts the TeV flux (or overpredicts the flux in the lower energy bands). There are several possibilities to explain this discrepancy. For instance, as suggested by Nayana et al. (2017), one can assume an ambient magnetic field that is lower by a factor of two in this region ($\sim 13 \mu\text{G}$) to reduce the relative flux at low energies. Alternatively, the TeV excess can be attributed to a higher seed photon density associated with the infrared emission from dust in the Galactic plane or to an additional hadronic component. In the latter case, even arbitrarily assuming the same normalisation for proton and electron populations, one can estimate the density of the target medium required to account for the discrepancy at $\sim 2000 \text{ cm}^{-3}$. We note that this is still reasonably low as the X-ray absorption is highest in this direction ($\sim 2 \times 10^{22} \text{ atoms cm}^{-2}$), and even higher density might be required to produce the observed CO emission (Maxted et al. 2015) (see also discussion in Sect. 3.3). The corresponding SED model is also shown in Fig. 6 for reference.

3.2. Correlation of $^{12}\text{CO}(J = 1-0)$ and X-ray absorption

H.E.S.S. Collaboration et al. (2011) estimated the distance to the source comparing the largest measured X-ray absorption column with the column density derived based on the velocity spectra of ^{12}CO (Dame et al. 2001) and HI (Haverkorn et al. 2006) emission. They concluded that these become comparable for velocities integrated up to a radial velocity relative to the local standard of rest (LSR) of -25 km s^{-1} . The corresponding peak in integrated column is located at -18 km s^{-1} , which corresponds to a lower limit on the distance of ~ 3.2 kpc. This estimate is qualitative, and in principle depends on the assumed composition of ISM and needs verification.

H.E.S.S. Collaboration et al. (2011) pointed out that for the same integration velocity the observed CO intensity increases in the direction of the Galactic plane similarly to the X-ray absorption. This conclusion can be verified quantitatively using the *XMM-Newton* spatially resolved spectroscopy. To do so we use the CfA survey (Dame et al. 2001) as used by H.E.S.S. Collaboration et al. (2011), and calculate the Pearson correlation coefficient between the observed X-ray absorption and the ^{12}CO column integrated up to a given velocity within a given spatial region. None of the published HI data cubes (Haverkorn et al. 2006) covers the entire remnant which complicates a similar analysis for this data set, due to the presence of edge artefacts in individual data cubes covering parts of the remnant. On the other hand, for a correlation analysis no additional assumptions on the ISM composition are required as we do not have to convert the observed ^{12}CO line intensity to the absorption column density and only rely on a spatial correlation

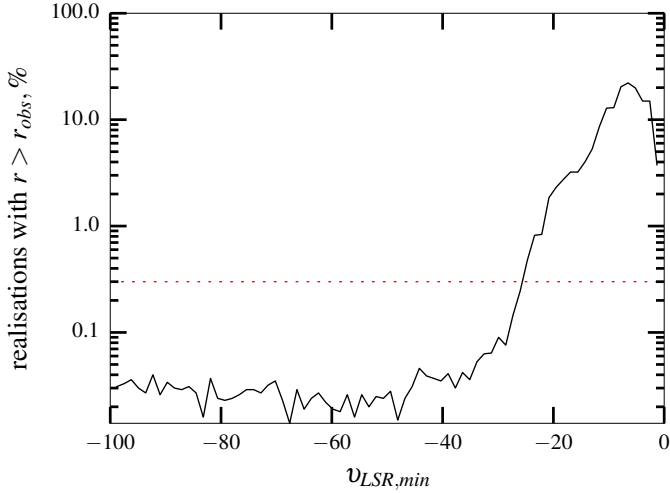


Fig. 7. Significance of the correlation between the absorption column density derived from *XMM-Newton* X-ray observations and the integrated CO temperature for different regions based on a permutation test (red dotted line indicates the 3σ level). The rapid drop in the correlation significance for $v_{\text{LSR}} \gtrsim -25 \text{ km s}^{-1}$ corresponds to a lower limit on distance of $\sim 3 \text{ kpc}$.

of the two quantities. To estimate the significance of the correlation in each case we compare the observed correlation coefficient with a respective sample of values obtained by shuffling the regions (i.e. a bootstrapping technique with 10^5 realisations). As illustrated in Fig. 7, the correlation is indeed significant for integration velocities $v_{\text{LSR}} \lesssim -20 \text{ km s}^{-1}$. We note that our result is based on ^{12}CO data which exhibits no significant features around this velocity, so the correlation is likely disrupted by an additional contribution from atomic hydrogen which appears around -18 km s^{-1} (H.E.S.S. Collaboration et al. 2011). This confirms the suggested similarity of X-ray absorption and column density maps (H.E.S.S. Collaboration et al. 2011) and reinforces their conclusions on the lower distance limit, although this analysis would certainly benefit from the detailed HI/ ^{12}CO mapping of the entire remnant.

It is interesting to note that a similar distance estimate can be obtained independently based on the analysis of the optical extinction known to be correlated with absorption in X-rays (Vuong et al. 2003). Using the 3D dust extinction mapping results presented by Schultheis et al. (2014), we estimated the average absorption as a function of distance in the direction of the remnant as shown in Fig. 8. Most of the absorbing material is concentrated at around 3 kpc, i.e. it coincides with the ^{12}CO emission peak at $v_{\text{LSR}} \sim -18 \text{ km s}^{-1}$. Unlike the radio data, this result does not depend on the Galactic rotation curve model. Finally, a distance of about 3.4 kpc for the remnant is also suggested from the red-clump method (Zhu et al. 2015; priv. comm.).

3.3. TeV, radio, and X-ray morphology of the shell

With the full remnant now covered also by X-ray observations, it becomes possible to compare the morphology of the shell in TeV, radio, and X-ray bands. The TeV and radio shells have been reported to have relatively flat azimuthal profiles (H.E.S.S. Collaboration et al. 2011), which does not seem to be the case for X-rays where the western part of the remnant is dimmer than the rest of the shell.

For a meaningful comparison, however, it is important to account for non-uniform absorption. The apparent blue tint of the false-colour mosaic image (Fig. 1) is mostly due to the absorption

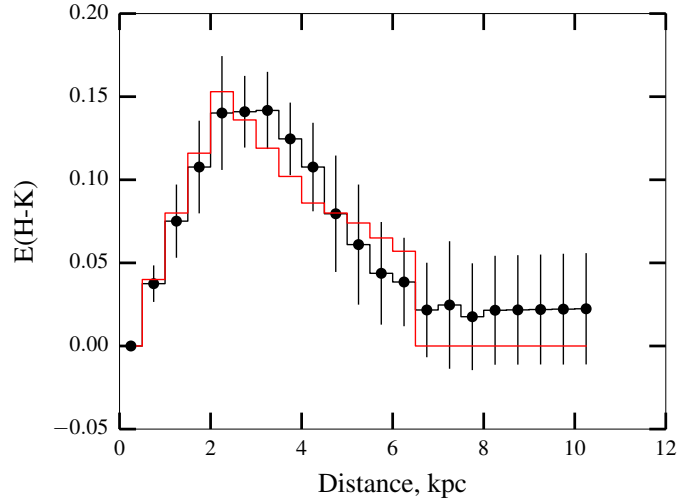


Fig. 8. Mid-infrared extinction as a function of distance in the direction of the remnant. The points and uncertainties correspond to mean and standard deviation of values reported by Schultheis et al. (2014) averaged within a circle with radius of 0.25° centred on the CCO. The red line shows the extinction as a function of distance for the dense filament marked in Fig. 11 (the respective uncertainties are not shown for clarity, but they are a factor of two smaller than for the black points).

of the soft flux by the interstellar medium and not to a significant change in hardness of the SNR emission, so the absorption is important. However, the overall impact of the absorption on the observed X-ray flux is minor as the shell spectrum is relatively hard and the absorption only varies by a factor of three. To better illustrate this point and enable a direct comparison of the X-ray shell morphology with other bands, we estimated the intrinsic X-ray flux based on the results of the spectral analysis. The corrected image reveals no significant variation in hardness of the extended emission as illustrated in the left panel of Fig. 9. The overall intensity of the X-ray flux and the shape of the shell are also not significantly affected, which is actually not surprising given the relatively hard spectrum of the shell and that the absorption column density only varies by factor of three across the remnant. We use, therefore, the full-band (0.4–10 keV) X-ray image for comparison with the radio and TeV maps.

The morphology in the radio band seems to depend on frequency (Nayana et al. 2017). However, a detailed analysis of the radio data is still ongoing, so we limit the comparison to the 325 MHz band where the shell seems to be best defined. For a quantitative comparison we also smooth all three maps with a $3.6'$ Gaussian kernel corresponding to the point spread function of the TeV map. We also excluded the bright HII region to the west of the remnant prior to convolution of the radio map, as illustrated in Fig. 9. Using the convolved maps, we obtained azimuthal surface brightness profiles for all three bands similar to those reported by H.E.S.S. Collaboration et al. (2011). Taking into account that the shell is well-defined in both X-ray and radio bands, we considered a ring with inner and outer radii of 0.18 and 0.24 degrees, respectively, rather than integrating the emission from the complete shell. The results are presented in Figs. 9 and 10 and indeed confirm the initial observation of X-ray dimming towards the western part of the remnant. Interestingly, the smoothed 325 MHz radio map seems to follow the same trend, and in general exhibits a behaviour similar to that in X-rays. On the other hand, the TeV emission shows no significant azimuthal variations with the western part being one of the brightest parts of the shell.

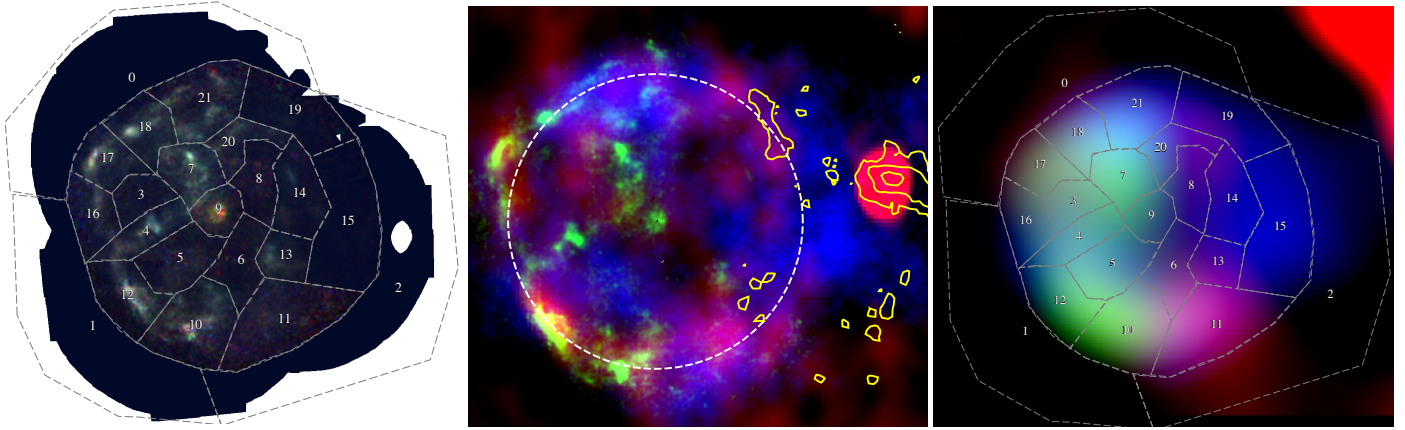


Fig. 9. X-ray image screened for point source contribution and corrected for the identified background components and absorption representing the intrinsic source flux (*left panel*). The bright blob in the centre of the X-ray shell is due to residual emission from the bright CCO. A comparison of the SNR shell morphology in radio (red, GMRT), X-ray (green, *XMM-Newton*), and TeV (blue, HESS) bands is shown in the *middle and right panels*. The dashed circle centred on the CCO indicates an approximate extension of the SNR shell based on the X-ray and radio intensity. The bright radio and X-ray filaments seem to be well correlated (*middle panel*). However, the radio shell is more symmetric and extends further towards the Galactic plane. There seems to be a correspondence between the continuum radio and sub-mm emission (yellow contour) tracing the cold dense region also noted by [Maxted et al. \(2015\)](#) in the CS MOPRA data. The *right panel* shows all three bands smoothed with a 0.06° Gaussian, corresponding to the PSF of the HESS data. We note region 15 at $l \sim 353.5$, $b \sim -0.5$ where the shell is only bright in TeV.

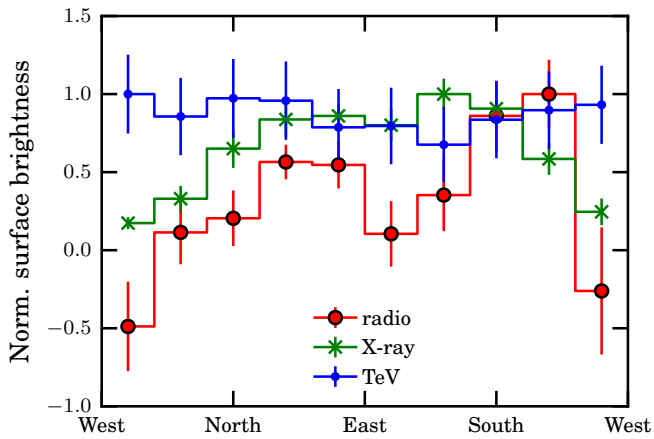


Fig. 10. Shell azimuthal surface brightness profile in TeV, X-ray, and radio bands. The shell is assumed to be centred on the CCO and have radius from 0.18° to 0.24° . The radio and X-ray images were smoothed with the HESS psf to allow meaningful comparison. X-ray and radio emission are both suppressed towards the Galactic plane (i.e. western or spectral extraction regions 15, 19), whereas the TeV profile is consistent with being flat.

3.4. Distance and association with the molecular cloud

As already mentioned, a rather robust lower limit on the distance can be obtained, due to the spatial correlation of the X-ray absorption and the ^{12}CO emission from material located in the Scutum-Crux arm at ~ 3 kpc. On the other hand, the observed TeV flux implies that the distance to the source cannot be much larger than that (i.e. not behind the Galactic centre). Most star forming regions trace the Galactic spiral arms, so this immediately triggered the idea that the remnant might be in the same arm and interact with the foreground molecular cloud. To confirm this hypothesis, however, an independent distance estimate to the source was needed, which proved to be more difficult.

The analysis of the X-ray spectrum of the central compact object suggests that distances larger than ~ 5 kpc imply uncomfortably large NS radii for the CCO in the centre of the remnant ([Klochkov et al. 2013, 2015](#)), so the remnant most likely resides

either in the Scutum-Crux (~ 3 kpc) or in the Norma-Cygnus (~ 4.5 kpc) Galactic arms.

The distance to the source can also be estimated by modelling the SED of a bright central star illuminating the recently discovered dust shell within the remnant that is also associated with the CCO ([Doroshenko et al. 2016](#)). In particular, for standard dust composition [Vickers et al. \(2015\)](#) estimate a distance of $3.8(7)$ kpc, i.e. close to the lower limit obtained above.

This estimate is barely consistent with the distance estimate of ~ 5.2 kpc obtained by [Fukuda et al. \(2014\)](#) based primarily on a qualitative comparison of the morphology of the TeV and HI radio emission. We note, however, that [Maxted et al. \(2015\)](#), using the higher resolution MOPRA data, detected no significant CS emission around $v_{\text{LSR}} = -85 \text{ km s}^{-1}$ suggested by [Fukuda et al. \(2014\)](#). On the other hand, [Maxted et al. \(2015\)](#) were able to detect several dense clumps of matter at $v_{\text{LSR}} \sim -15 \text{ km s}^{-1}$ (corresponding to a distance of ~ 3 kpc) seemingly aligned with the SNR shell as observed in radio continuum. It is interesting to note that this velocity is close to the peak in ^{12}CO emission at $\sim -18 \text{ km s}^{-1}$, which, as discussed above, is associated with the bulk of matter responsible for the X-ray absorption.

Higher resolution MOPRA maps presented by [Maxted et al. \(2015\)](#) show that the velocity of the denser clumps tracing the western rim of the SNR deviates slightly from that for the bulk of the surrounding material. A similar behaviour is, in fact, also observed in other interacting SNRs ([Moriguchi et al. 2005; Castelletti et al. 2013](#)), and thus can be viewed as an argument for the physical association of HESS J1731–347 with the molecular cloud at $\sim -18 \text{ km s}^{-1}$. The absence of such peculiarities in the velocity of the nearby material was quoted by [Nayana et al. \(2017\)](#) as an argument against the interaction of the SNR with nearby molecular clouds, which thus does not hold. It should be noted, however, that this argument was motivated by [Dame et al. \(2001\)](#) data which has limited spatial resolution, so it would be hard to notice any peculiarities in the first place. The main issue with this argument is that the mechanisms responsible for acceleration of clumps are unclear, and that the clumps themselves are rather compact, so there is a possibility of a random spatial coincidence with the shell. This possibility could be ruled out with more sensitive and higher resolution radio observations which would more

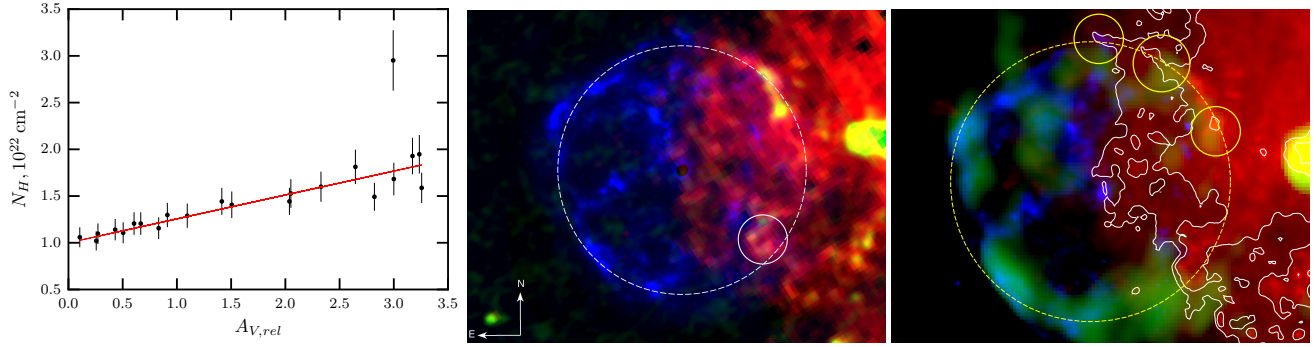


Fig. 11. Correlation of the absorption column measured from the spatially resolved spectral analysis of *XMM-Newton* data and the relative reddening derived from VVV photometry (*left panel*). The outlier point corresponds to region 2 where the optical extinction is underestimated due to the lack of stars in the optical data. We find $N_{\text{H}} \sim 1 + A_{\text{V,rel}}/4$ from a linear fit including a 10% systematic uncertainty for the column measured in X-rays. A composite image of the calibrated absorption column density map derived from optical extinction (red) and ATLASGAL 0.87 mm (green) maps is shown together with the X-ray 0.4–10 keV image (blue) for reference in the *middle panel*. We note the enhanced absorption along the western rim of the remnant, particularly along its north-western part. The same features can be traced in the composite image showing X-ray (blue), radio (green), and 350 μm *Herschel*/SPIRE data (*right panel*). The white contours correspond to *Herschel* data to highlight the extension of the filament in the north-west in northern direction where it bridges with the X-ray filament as shown with the northernmost yellow circle (see also the *middle panel* where the X-ray filament is more clearly seen). The other two circles emphasise the correspondence between the infrared and radio data along the filament.

accurately trace the western rim of the SNR both in lines and continuum.

Here we add that to some extent the alignment of the dense clumps with the SNR shell can be confirmed by an analysis of data from other wavelengths. In particular, the dense clumps traced by CS emission can also be observed as a thin dark filament in *Spitzer* MIPS/IRAC data (Doroshenko et al. 2016, see Fig. 1), and in submillimetre emission in the ATLASGAL survey (Schuller et al. 2009) as illustrated in Fig. 9. Moreover, the same structure can also be detected in optical extinction maps where it can be traced along the entire western part of the remnant, and seems to be perfectly aligned with the detected X-ray shell in the north-west. While this does not unambiguously prove their association, such a coincidence seems unlikely to be just by chance.

To estimate the column density from optical reddening we used the recently released *PNICER* package (Meingast et al. 2017), and photometry from the VISTA VVV survey (Minniti et al. 2010). The extinction map with an angular resolution of 1' was produced using the mid-infrared colours and the spectral extraction region 1 as a reference field. The result was then calibrated to the neutral column density using the absorption column densities measured across the remnant using *XMM-Newton* data as illustrated in Fig. 11. It is important to emphasise that the X-ray absorption and optical extinction are closely correlated, with the sole exception of region 2 where the extinction is underestimated due to the strong absorption. The resulting absorption map is closely correlated with the sub-mm emission coming from the most absorbed areas (which also coincides with the CS emission in radio), and arguably better illustrates the alignment of the absorbing material with the northern edge of the remnant. The individual clumps detected in the CS and sub-mm bands also correspond to the strongest extinction; however, a less intense rim connecting them is also visible in the extinction map. We note that the filament detected in CS/sub-mm in regions 15–19 extends further to the north in the extinction map, and is aligned with the X-ray shell.

It is interesting to note that in the infrared band, these filaments are clearly observed to be in the foreground with respect to the bulk of the emitting material (see Fig. 1 in Doroshenko et al. 2016), which is likely associated with the CO emitting material and is thus responsible for the X-ray absorption. The 3D mapping of the mid-infrared extinction by Schultheis et al. (2014) seems

to support this observation, although the resolution of the published maps is probably insufficient to draw any firm conclusions. Nevertheless, the larger filament in the south-west marked with a circle in Fig. 11 has a comparable size to and is aligned with the filament shown in the 3D extinction map sky pixels presented by Schultheis et al. (2014). As shown in Fig. 8, the distribution of matter in this direction is similar to that within the entire remnant, which suggests that the bulk of the absorbing material in the filament must be relatively close to the larger cloud. However, the distribution seems to be slightly skewed to the front, which could explain why the filaments appear dark in the infrared.

On the other hand, as concluded above, the filament seems to be aligned with the western rim of the SNR and thus is at the same distance as the remnant itself. However, the remnant must be in the background of the material absorbing X-ray and optical emission. There is, therefore, an apparent contradiction since the remnant and the filament cannot be in front of and behind the molecular cloud at the same time. This is possible if the apparent alignment is still a chance coincidence or if the remnant and the molecular cloud responsible for the absorption of the observed X-ray emission are actually at the same distance and interact with each other. In this case the fact that part of the shell appears in the foreground could be explained by irregularities in the distribution of material within the absorbing cloud.

This conclusion is supported by the fact that no significant X-ray emission is detected from the western part of the remnant. Indeed, there is an apparent difference in the X-ray morphology in the eastern and western parts which needs to be explained. The easiest explanation is then that the SNR shock encountered dense material in the west and slowed to the point when synchrotron falls out of the X-ray band (keeping in mind that radio emission is still observed from the region). This scenario has in fact been discussed by Cui et al. (2016), who suggested that the observed X-ray synchrotron emission from the shell requires high shock velocities, which can only be retained if the remnant expands into an essentially empty stellar bubble blown by the progenitor. The absence of X-ray emission from the western part suggests that the shock velocity is much lower there, pointing to interaction with dense molecular clouds. If this is indeed the case, the interaction must have started quite recently since otherwise the circular shape of the radio and TeV shells would also have been distorted. Furthermore, once the interaction starts the strong shock

must start heating the swept-up material, eventually producing thermal X-ray emission which has not yet been detected.

We note that in the case of the SNR RX J1713.7–3946, which displays a similar large-scale X-ray intensity trend, a different scenario has been invoked. There, the X-ray brightening has been interpreted as coming from an interaction with molecular clouds, while the dimmer part has been associated with lower density surrounding material [Cassam-Chenaï et al. \(2004\)](#). In the case of HESS J1731–347, this interpretation is not supported by the available gas density tracers. Also, the TeV emission in the west of the SNR which does not follow the dimming trend would need to be explained by processes not directly related to the SNR. A more straightforward explanation is therefore opposite to RX J1713.7–3946, namely that the SNR shock encountered dense material in the X-ray dim regions.

Alternatively, the absence of bright filaments in the western part could be explained as being projection effects. However, this also requires interaction with the inhomogeneous medium. We conclude, therefore, that the possibility that the remnant interacts with the cloud is consistent with observations, and this region is thus a plausible target to search for high energy hadronic emission. In particular, it would be important to search for changes in the TeV spectrum in the western part of the remnant with additional VHE observations. Indirect evidence can also be obtained based on deeper radio observations aimed to better constrain suggested changes of the spectral index, and independently estimate the magnetic field as discussed by [Nayana et al. \(2017\)](#).

4. Conclusions

XMM-Newton observations of the SNR HESS J1731–347 covered the entire shell visible in TeV and radio bands for the first time. In the X-ray band, the morphology of the remnant is quite irregular: the eastern part is considerably brighter than the western part (which is closer to the Galactic plane). The emission from the eastern part is dominated by narrow, well-defined filaments correlated with radio emission, whereas the western part is dimmer and more diffuse. A spatially resolved spectral analysis confirmed the previously reported ([H.E.S.S. Collaboration et al. 2011](#)) non-thermal origin for the X-rays. The increase in the absorption column towards the Galactic plane is correlated with the CO emission observed in radio, which puts a lower limit on the distance to the source of $\sim 3.2\text{--}4$ kpc. This estimate is consistent with the observed velocities of dense CS clumps reported by [Maxted et al. \(2015\)](#), which indeed seem to be tracing the western rim of the shell.

Based on the updated X-ray and radio fluxes, we find that the broadband spectral energy distribution is consistent with synchrotron in the radio to X-ray and inverse Compton in the TeV bands, although the morphology of the shell in the respective bands seems to be slightly different. In particular, the X-ray and radio continuum emission is suppressed towards the Galactic plane, which is not the case for the TeV emission where the shell shows a flat azimuthal profile. Taking into account the CS emission and enhanced optical extinction along the western part of the remnant, we conclude that the remnant is most likely interacting with the nearby dense molecular cloud. This conclusion supports the SNR evolution scenario outlined by [Cui et al. \(2016\)](#), and might signify that part of the observed TeV emission actually has a hadronic origin.

Based on the spatially resolved spectral analysis of the extended emission we do not find, however, any significant

variations in the intrinsic X-ray spectrum of the shell, which could be expected for a remnant interacting with the non-uniform ISM. On the other hand, minor variations in the X-ray spectrum still cannot be completely excluded due to the strong stray-light contamination affecting the *XMM-Newton* data. Furthermore, the brightness of the shell in the western part is not sufficient for a detailed spectral analysis. The fact that it is so low can be interpreted as an argument supporting the interaction of the shell with the cloud. Finally, we also find no evidence for thermal emission from the ejecta or reverse shock. The latter is not surprising given the amount of cold dust observed within the shell.

Acknowledgements. The authors would like to thank the Deutsches Zentrum für Luft- und Raumfahrt (DLR) and Deutsche Forschungsgemeinschaft (DFG) for financial support (grants DLR 50 OR 0702, FKZ 50 OG 1301, SA2131/1-1, FKZ OR 1310). W. W. Tian acknowledges support from the NSFC (11473038). A.B. acknowledges support from the Grant-in-Aid for Scientific Research of the Japanese Ministry of Education, Culture, Sports, Science and Technology (MEXT) of Japan, No. 15K05107. The authors thank the anonymous referee for the timely and useful comments which helped to improve the manuscript.

References

- Acero, F., Lemoine-Goumard, M., Renaud, M., et al. 2015, *A&A*, **580**, A74
 Bamba, A., Yamazaki, R., Ueno, M., & Koyama, K. 2003, *ApJ*, **589**, 827
 Bamba, A., Yamazaki, R., Yoshida, T., Terasawa, T., & Koyama, K. 2005, *ApJ*, **621**, 793
 Bamba, A., Pühlhofer, G., Acero, F., et al. 2012, *ApJ*, **756**, 149
 Berezhko, E. G., & Völk, H. J. 2008, *A&A*, **492**, 695
 Cappelluti, N., Brusa, M., Hasinger, G., et al. 2009, *A&A*, **497**, 635
 Cassam-Chenaï, G., Decourchelle, A., Ballet, J., et al. 2004, *A&A*, **427**, 199
 Castelletti, G., Supan, L., Dubner, G., Joshi, B. C., & Surnis, M. P. 2013, *A&A*, **557**, L15
 Cui, Y., Pühlhofer, G., & Santangelo, A. 2016, *A&A*, **591**, A68
 Dame, T. M., Hartmann, D., & Thaddeus, P. 2001, *ApJ*, **547**, 792
 Doroshenko, V., Pühlhofer, G., Kavanagh, P., et al. 2016, *MNRAS*, **458**, 2565
 Ebisawa, K., Yamauchi, S., Tanaka, Y., et al. 2008, *PASJ*, **60**, S223
 Fukuda, T., Yoshiike, S., Sano, H., et al. 2014, *ApJ*, **788**, 94
 Gabici, S., & Aharonian, F. A. 2014, *MNRAS*, **445**, L70
 Haverkorn, M., Gaensler, B. M., McClure-Griffiths, N. M., Dickey, J. M., & Green, A. J. 2006, *ApJS*, **167**, 230
 H.E.S.S. Collaboration, Abramowski, A., Acero, F., et al. 2011, *A&A*, **531**, A81
 Klochkov, D., Pühlhofer, G., Suleimanov, V., et al. 2013, *A&A*, **556**, A41
 Klochkov, D., Suleimanov, V., Pühlhofer, G., et al. 2015, *A&A*, **573**, A53
 Maxted, N., Rowell, G., de Wilt, P., et al. 2015, ArXiv e-prints [[arXiv:1503.06717](#)]
 Meingast, S., Lombardi, M., & Alves, J. 2017, *A&A*, **601**, A137
 Minniti, D., Lucas, P. W., Emerson, J. P., et al. 2010, *New Astron.*, **15**, 433
 Moriguchi, Y., Tamura, K., Tawara, Y., et al. 2005, *ApJ*, **631**, 947
 Morrison, R., & McCammon, D. 1983, *ApJ*, **270**, 119
 Nayana, A. J., Chandra, P., Roy, S., et al. 2017, *MNRAS*, **467**, 155
 Revnivtsev, M., Sazonov, S., Gilfanov, M., Churazov, E., & Sunyaev, R. 2006, *A&A*, **452**, 169
 Schuller, F., Menten, K. M., Contreras, Y., et al. 2009, *A&A*, **504**, 415
 Schultheis, M., Chen, B. Q., Jiang, B. W., et al. 2014, *A&A*, **566**, A120
 Tian, W. W., Leahy, D. A., Haverkorn, M., & Jiang, B. 2008, *ApJ*, **679**, L85
 Tian, W. W., Li, Z., Leahy, D. A., et al. 2010, *ApJ*, **712**, 790
 Uchiyama, Y., Aharonian, F. A., Tanaka, T., Takahashi, T., & Maeda, Y. 2007, *Nature*, **449**, 576
 Valinia, A., & Marshall, F. E. 1998, *ApJ*, **505**, 134
 Vickers, S. B., Frew, D. J., Parker, Q. A., & Bojičić, I. S. 2015, *MNRAS*, **447**, 1673
 Vuong, M. H., Montmerle, T., Grosso, N., et al. 2003, *A&A*, **408**, 581
 Yang, R.-Z., Zhang, X., Yuan, Q., & Liu, S. 2014, *A&A*, **567**, A23
 Yuasa, T., Makishima, K., & Nakazawa, K. 2012, *ApJ*, **753**, 129
 Zabalza, V. 2015, *Proc. of International Cosmic Ray Conference 2015*, 922
 Zhu, H., Tian, W. W., & Wu, D. 2015, *MNRAS*, **452**, 3470